Non-linear magnetohydrodynamic simulations of density evolution in Tore Supra sawtoothing plasmas

T. Nicolas, R. Sabot, X. Garbet, H. Lütjens, J.-F. Luciani, Z. Guimaraes-Filho, J. Decker, A. Merle

Non-linear magnetohydrodynamic simulations of density evolution in Tore Supra sawtoothing plasmas

T. Nicolas,[1] R. Sabot,[1] X. Garbet,[1] H. Lütjens,[2] J.-F. Luciani,[2] Z. Guimaraes-Filho,[3,4] J. Decker,[1] and A. Merle[1]
[1]*CEA, IRFM, F-13108 Saint-Paul-Lez-Durance, France*
[2]*Centre de Physique Théorique, Ecole Polytechnique, CNRS, F-91128 Palaiseau Cedex, France*
[3]*Aix-Marseille University, IIFS-PIIM, UMR 7345, F-13397 Marseille, France*
[4]*Instituto de Física, Universidade de São Paulo, São Paulo, Brazil*

(Received 3 October 2012; accepted 26 October 2012; published online 28 November 2012)

The plasma density evolution in sawtooth regime on the Tore Supra tokamak is analyzed. The density is measured using fast-sweeping X-mode reflectometry which allows tomographic reconstructions. There is evidence that density is governed by the perpendicular electric flows, while temperature evolution is dominated by parallel diffusion. Postcursor oscillations sometimes lead to the formation of a density plateau, which is explained in terms of convection cells associated with the kink mode. A crescent-shaped density structure located inside $q=1$ is often visible just after the crash and indicates that some part of the density withstands the crash. 3D full MHD nonlinear simulations with the code XTOR-2F recover this structure and show that it arises from the perpendicular flows emerging from the reconnection layer. The proportion of density reinjected inside the $q=1$ surface is determined, and the implications in terms of helium ash transport are discussed. © *2012 American Institute of Physics*. [http://dx.doi.org/10.1063/1.4766893]

I. INTRODUCTION

The issue of sawteeth is of significant importance in the physics of tokamaks, for several reasons. First, sawteeth provide a way of studying magnetic reconnection in laboratory plasmas, and there still remains a lot to be discovered on this topic. The theory of reconnection in tokamaks has generated numerous developments, e.g.,[1–12] but despite all this effort, some features of the sawtooth instability remain mysterious, such as the very short duration of the collapse phase. Hence, sawteeth still deserve attention. Also, purely in terms of tokamak operation, sawteeth are a double-edged sword. On the one side, each sawtooth crash reduces the core temperature and density by typically 10%.[13] Since the fusion power scales as the square of the pressure of the deuterium-tritium mixture, it is seen that a sawtooth crash can transiently reduce the efficiency of the fusion reactions by up to 35%. Furthermore, energetic particle populations like the 3.5 MeV α-particles are found to stabilize sawteeth, making their period longer.[14] This can lead to a stronger crash (monster sawteeth), able to trigger secondary instabilities like neoclassical tearing modes.[15] Thus, sawteeth are a hindrance to good plasma operation. On the other side, the inert α-particles continuously produced by the fusion reactions need to be evacuated before they choke the plasma by diluting it. For instance, given the target fusion power in ITER, 500 MW, and the expected sawtooth period, >10 s for monster sawteeth,[14] the amount of mixture converted to α-particles between two crashes reaches a few percents. The thermalized fast particles build-up inside the $q=1$ surface, which acts like a transport barrier, and are released only at the onset of the crash. Here, q is the inverse of the twist number of magnetic field lines, called safety factor. Thus, sawteeth provide a possible mechanism to wash the core from the helium ash.[16,17]

However, it appears that the issue of the particle transport induced by the sawtooth has not been thoroughly studied. Most sawtooth observations in the past used X-ray[18–21] imaging, electron cyclotron emission (ECE) imaging,[19,22,23] or Thomson scattering,[5,24,25] to study the impurity content and the electron temperature, but there has not been much focus on the electron density itself. The density and temperature profiles are most often assumed to be completely flattened by the sawtooth crash.[14] In this paper, we present new elements based on recent experimental and numerical results drawing a different picture. Experimental results are obtained using fast-sweeping X-mode reflectometry[26,27] for the density and ECE for the temperature, while numerical simulations are carried out with the full MHD 3D non-linear XTOR-2F[28–30] code.

It is found that the transport of particles during the crash itself is mainly governed by the poloidal perpendicular flows. The density structures observed in the experiment are recovered in the simulations. The XTOR-2F code has been used to understand the mechanism of their formation. A significant part of the core density in excess of the density at the $q=1$ surface is not expelled but instead is reinjected inside the $q=1$ surface. Following this mechanism, a crescent-shaped density structure is obtained, which is clearly visible both in the experiment and in the simulation.

The paper is organized as follows. In Sec. II, the experimental methods and results are presented and discussed. In Sec. III, the numerical methods are considered. In Sec. IV, the physical analysis of experiments and simulations is carried out. Finally, the implications of the results are discussed in Sec. V.

II. EXPERIMENTAL RESULTS

Reflectometry has been used for decades to scan the electron density of the plasma. It is based on the principle that electromagnetic waves can only propagate if their frequency is higher than a critical pulsation ω_c. Below ω_c, the wave is evanescent. Thus, a wave with frequency ω is launched into the plasma. When the propagating wave reaches the cut-off layer where $\omega_c = \omega$, it is reflected. The detection of the phase of the wave gives access to the time of flight, then yielding the position of the cut-off layer r_c. Whenever ω_c is a known function of the density n_e, the position of the cut-off layer yields the couple $(n_e; r_c)$. If several waves with different frequencies are launched in the plasma, a density profile may be reconstructed. The critical pulsation depends on the polarization of the wave. In the ordinary (O) mode, it is equal to the plasma pulsation $\omega_{pe} = \sqrt{n_e e^2/\varepsilon_0 m_e}$. The critical pulsation increases monotonically with n_e, so that peaked profiles can be scanned only on the low field side of the tokamak, where the reflectometer is located. In the extraordinary (X) mode, there are two cut-off pulsations ω_c^6, which have a dependence on the cyclotron pulsation $\omega_{ce} = eB/m$. The upper X-mode is used, $\omega_c = \frac{1}{2}\sqrt{\omega_{ce}^2 + 4\omega_{pe}^2} + \omega_{ce}$, which takes advantage of the $1/R$ dependence of the magnetic field, due to toroidicity. Using X-mode instead of O-mode allows to reach the high field side even for peaked profiles. Fig. 1 displays a peaked density profile of the Tore Supra shot #44634, and the corresponding cut-off frequencies. It is seen that in O-mode, the plasma cannot be scanned for major radii smaller than 2.4 m, whereas in X-mode, it can be scanned for radii in the range [1.7 m, 3.1 m]. However, the frequencies needed are much higher, in the range [100 GHz, 150 GHz].

Fast-sweeping of the probe frequency yields a density profile in 40 μs. There is a delay of 5 μs between two measurements. The profile is iteratively reconstructed and the relative error on the measurement is below 1%. The radial resolution is 1.2 cm. The structures observed using the reflectometry technique are assumed to rotate in the poloidal plane. In the experiments analyzed in this work, the frequency of the sawtooth precursor, identified as an $m/n = 1/1$ internal kink, is observed to be close to 1 kHz. Here, m and n are the poloidal and toroidal wave numbers. The measured frequency $\Omega/2\pi$ is the sum of the rotation frequency of the plasma.[31] and of the internal kink frequency $\omega/2\pi$. The ratio

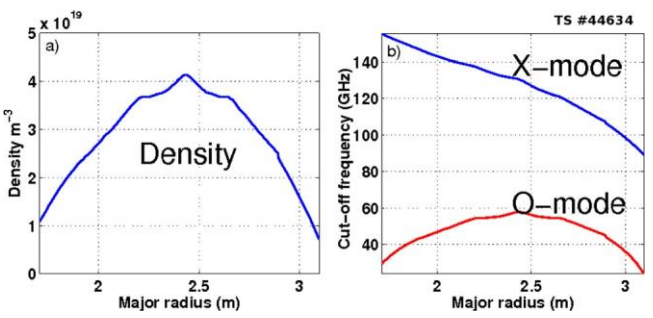

FIG. 1. Typical peaked density profile (a) on Tore Supra shot #44634, and corresponding cut-off frequency, in O-mode and X-mode (b).

between the plasma period and the total sampling time of 45 μs is close to 22, so that tomographic inversion can be carried out.[27]

The technique used here to perform tomographic reconstructions is similar to that used in Ref. 32. The poloidal plane is described by a polar mesh $(r; h)$. The experimental profiles give the density on the line $h = 0$. The pulsation ω_0 of the mode is first evaluated. Then, the density at h_0 at a time t_0 is the mean of the density at $h = 0; t = t_0 - h_0/\omega_0$ with weight $p - h_0$ and of the density at $h = p; t = t_0 + (p - h_0)/\omega_0$ with weight h_0, in order to reflect proximity in time. In other words, the density is an interpolation between what the density was h_0/ω_0 seconds before and what it is known to be $(p - h_0)/\omega_0$ seconds later.

An example of this technique applied to a Tore Supra plasma is shown on Fig. 2. The plasma parameters are as follows: magnetic field on axis $B_0 = 3.8$ T, minor radius $a = 0.72$ m, major radius $R_0 = 2.4$ m, core density $n_0 = 3.8 \times 10^{19}$ m^{-3}, core electronic temperature $T_{e0} = 2.4$ keV, poloidal beta (for a parabolic pressure profile) $\beta_p = l_0(R_0/a)^2 n_0 T_{e0}/B_0^2 = 0.01$, plasma current $I_P = 1.2$ MA, ohmic heating (no additional heating powers). The sequence can be described as follows:

- A: after a crash, the density is almost flat inside the $q = 1$ surface and a peaking is seen to appear in the deepest core.
- B: a kink oscillation appears and the peaked core is displaced.
- C: The kink does not lead to a sawtooth crash but is later stabilized. Let us denote this a partial crash. The peak thus continues to grow.
- D: The peak is highest just before new kink oscillations appear in the core, this time leading to a sawtooth crash.
- E: After the sawtooth crash, a very distinct crescent-shaped density structure can be observed inside the $q = 1$ surface. It must have formed during the reconnection phase because it is present immediately after the crash.
- F: After a few milliseconds, the crescent-shaped structure is seen to homogenize poloidally, while the peaking reappears in the center of the image. The main ring (orange) is encircled by a secondary ring (light blue).

Fig. 3 displays the core density profiles together with the electron temperature measured using electron cyclotron emission, during the same shot, but 150 ms later ($t = 5.15$–5.17 ms).

These measurements deserve several comments. The density behaviour may seem unusual, compared to typical profiles obtained with interferometry. Recall, however, that the discharge is ohmic, with no additional heating or non-inductive current drive, hence there is a significant Ware pinch effect[33] due to the significant inductive toroidal electric field, responsible for density peaking inside the $q = 1$ surface. The Ware pinch is an inward radial velocity linked with the conservation of the canonical toroidal momentum under the hypothesis of axisymmetry. After the sawtooth crash, the density profile is flat, up to a few percents (*cf.* Fig. 3(c)), blue profile). The growth of the peaking can be observed while the density rebuilds on Fig. 3(c)). It was shown in Ref. 34 that indeed the measured pinch velocity

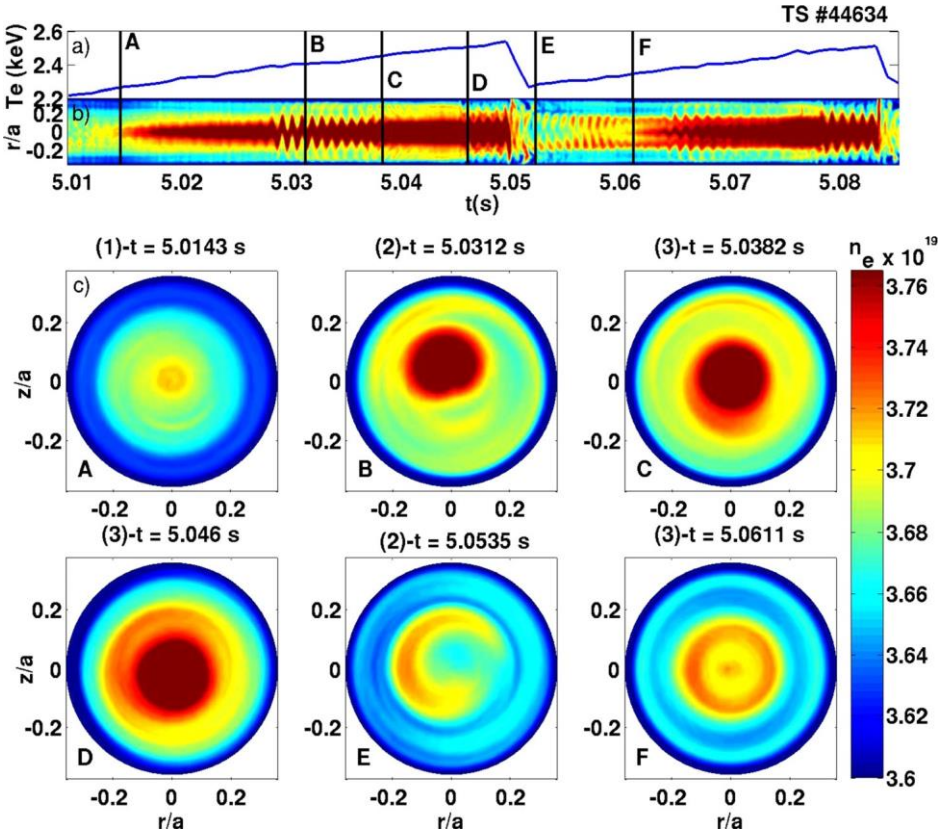

FIG. 2. Tore Supra shot #44634. Evolution of the central temperature (a), time trace of the reflectometry signal (b), and tomographic reconstructions of the plasma electronic density during a sawtooth (c). Vertical lines indicate the times at which snapshot is taken.

essentially agrees with the neoclassical calculation, obtained with the NCLASS code.[35] Reference 34 simultaneously measures the pinch velocity and diffusion coefficient inside the $q = 1$ surface by locally measuring the radial electron flux $C_e(r) = -1/r \int_0^r r' \partial_t n_e(r') dr'$ and plotting C_e/n_e versus $-\partial_r n_e/n_e$. When the particle source is negligible, this yields a straight line with slope D, the particle diffusion coefficient, and intersect V_p, the radial velocity pinch. The radial velocity is measured to be of the order of $0.1\ \mathrm{m\ s^{-1}}$, and can be considered as a constant except in the center where it drops to zero, thus avoiding singularity. The diffusion coefficient is of the order of $0.05\ \mathrm{m^2\ s^{-1}}$.

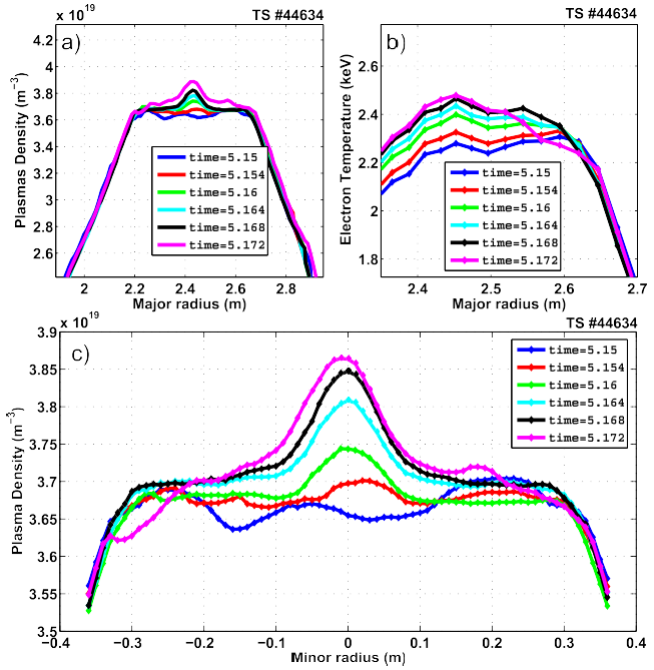

FIG. 3. Density profiles temperature profiles versus major radius in TS # 44634, for $t = 5.15$–5.17 ms, during the ramp phase of the sawtooth (a), corresponding electron temperature profiles obtained by ECE measurements (b). Zoom on the core density inside the $q = 1$ surface (c).

The shape of the building profile is remarkable: the profile is significantly more peaked deep inside than close to the $q = 1$ surface. Together with the steep gradients outside $r_s = q(r) = 1$ is yields the shape of a sombrero. This general shape can readily be explained. To simplify the discussion, we take a constant radial pinch velocity profile, which is realistic for $r > 0.05$ m. The evolution of the electron density n_e is modeled with a convection diffusion equation:

$$\partial_t n_e = -\nabla \cdot (n_e V_p - D \nabla n_e); \tag{1}$$

where V_p is the constant pinch velocity and D the constant diffusion coefficient. Equilibrium yields the slope $|\nabla n_e/n_e| = |V_p/D|$, which is constant. However, in cylindrical geometry, the evolution towards this equilibrium is not uniform. Indeed volume effects yield an additional term $-n_e V_p/r$, in addition to advection $-V_p \cdot \nabla n_e$, which enhances the effect of the pinch close to the magnetic axis. As a result, the profile is more peaked in the center. This can be very easily verified numerically.

However, there is more to this than only radial convection. The previous simple model would be sufficient to

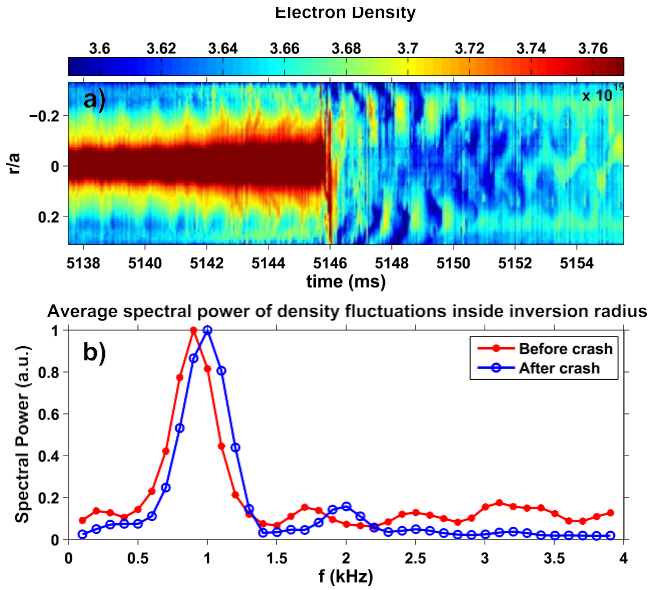

FIG. 4. Time trace of the equatorial density in Tore Supra ohmic shot #44634, obtained with fast-sweeping reflectometry (a), average spectral power of density fluctuations inside inversion radius (b).

describe the evolution of the profile if the latter was already flat immediately after the crash. However, the crash does not flatten the density profile completely. Structures of amplitude in the range of 1%–2% and of typical radial size equal to 0.2 m are obtained at the end of the reconnection phase, as seen on the blue profile, Fig. 3(c)). The first steps of the profile evolution are dominated by the obliteration of these structures, leading to the green profile. This process lasts 10 ms, so that a high diffusion of 4 m s^{-2} is required for a diffusive process to explain this flattening. Furthermore, if some turbulent process were responsible for such a rise in the perpendicular particle diffusion coefficient (compared to the aforementioned value of 0:05 m s^{-2}), the temperature diffusivity $\chi_\perp$ would also undergo a dramatic rise. As a result, the temperature profile would flatten significantly. Fig. 3(b)) shows, however, that the smooth evolution of the temperature profile is not affected during this. Finally, it is important to note that a magneto-hydrodynamic mode with mode numbers $m/n = 1/1$ is observed during the flattening. Fig. 4(a)) displays the time trace of the density, and Fig. 4(b)) the corresponding average power spectra, exhibiting the frequency of the mode preceding and following the crash. It is observed that the postcursor frequency ($t = 5.146$–5.150 s) is very close to the precursor frequency ($t = 5.140$–5.146 s). The precursor is a kink mode with frequency of the order of half the diamagnetic frequency χ^2, according to Ref. 36. The frequency of the plasma flows is also of the order of the diamagnetic frequency, so we can conjecture that both mode frequency and Doppler shift play significant roles in the total frequency in the laboratory frame. This conjecture will be checked in Sec. IV. Since the frequency of the postcursor is not different from that of the precursor, we can conclude that it is not the result of the mere convection of a residual density perturbation by the plasma rotation, but really the signature of kink type MHD activity following the crash. Such MHD activity can for instance be due to incomplete reconnection. It is important to note this fact because the flows affecting the density are very different in the presence or in the absence of MHD activity, as we will see in Sec. IV.

We now turn our attention to the crescent-shaped structure observed on frame E of Fig. 2(c)). It is very common in this kind of ohmic shot and is always observed immediately after the crash. It is as such remarkable that a clearly visible structure with definite shape is observed at the end of the reconnection phase, which is traditionally said to completely flatten the profiles. Frame F reveals that the crescent homogenizes poloidally to form a ring-shaped structure, in just a few rotation times. The peaking of the density can be seen to reappear in the deepest core on frame F.

We now review the numerical methods used to analyze these experimental results.

III. NUMERICAL METHODS

A. The XTOR-2F code

The XTOR-2F code is a nonlinear and bi-fluid full MHD code. It uses a fully implicit scheme to solve the following set of equations:[28]

$$\partial_t n + \nabla\cdot(n\mathbf{v}) = \nabla\cdot\left(\frac{\nabla p_i}{eB}\times\frac{\mathbf{B}}{B^2}\right) + S_n + \nabla\cdot(D_\perp\nabla n - V_p n); \tag{2}$$

$$nm_i(\partial_t + \mathbf{v}\cdot\nabla)\mathbf{v} = -\nabla p + \mathbf{J}\times\mathbf{B} + \nabla\cdot(\mu\nabla_\perp^2\mathbf{v}_i); \tag{3}$$

$$\partial_t p + \mathbf{v}\cdot\nabla p + C p\nabla\cdot\mathbf{v} = \nabla\cdot\left(\frac{p}{en}\nabla p\times\frac{\mathbf{B}}{B^2}\right) + \dots + \nabla\cdot(\chi_\perp\nabla_\perp p + n\chi_\parallel\nabla_\parallel T - \mathbf{v}_\perp\nabla_\perp^2 p); \tag{4}$$

$$\partial_t \mathbf{B} = \nabla\times(\mathbf{v}\times\mathbf{B}) + \nabla\times\left(\frac{\nabla_\parallel p_e}{en}\right) - \nabla\times\eta\mathbf{J}. \tag{5}$$

Here, $\mathbf{v} = \frac{\mathbf{E}\times\mathbf{B}}{B^2} + \mathbf{v}_\parallel$; $\mathbf{v}_i^* = -\frac{1}{neB^2}\mathbf{B}\times\nabla p_i$ designates the ion diamagnetic velocity, i and e the ion and electron populations, S_n is a particle source that is vanishing in the core, S_H is a heating source, C is the ratio of specific heats, $\chi_\parallel$ and $\chi_\perp$ are the parallel and perpendicular diffusivities, $D_\perp$ and V_p are the particle diffusion coefficient and radial pinch velocity, η is the resistivity, μ is the viscosity, and $n = n_i = n_e$ (quasi-neutrality). The difference between electron and ion temperatures is controlled by the parameter $s = T_i/T_e$, which is assumed constant and uniform. All our simulations assume $s = 1$. The fourth term in the l.h.s. of Eq. (2) is the divergence of the diamagnetic flux. Diamagnetic effects account for plasma rotation and for the real frequency of the kink mode. They also play a crucial role in accelerating reconnection during a sawtooth crash, through the second term in the l.h.s. of Eq. (5).[37,38] Halpern *et al.* demonstrated in Ref. 37 that two regimes of internal kink reconnection cycles are accessible with XTOR-2F, depending on the relative values of the resistivity and the diamagnetic effects. Namely, at low resistivity and with important diamagnetic effects, the system jumps from Kadomtsev-like smooth reconnection to a

regime of accelerated reconnection. The simulations presented here investigate this latter regime.

The code is spectral in poloidal and toroidal directions, and finite differences in the radial direction. Our simulations are carried out using 32 poloidal sections and 12 toroidal sections. Because of aliasing constraints, the number of modes with such a resolution is restricted to 4 toroidal modes ($n = 0, \ldots, 3$) and 9 poloidal modes ($m = 0, \ldots, 8$) (for the $n = 1$ component). The radial resolution is 200 grid points. It is determined by the condition $\Delta r \leq d$, where d is the width of the inertial layer in the reconnection region, and Δr is the radial step. Since $d \propto \eta^{1/3}$ when $\eta \to 0$, decreasing resistivity demands increasing the radial resolution. In XTOR-2F, the parameter controlling resistivity is the Lundquist number $S = \tau_R/\tau_A$, where $\tau_R = \mu_0 a^2/\eta$ is the resistive time and $\tau_A = \mu_0 n_0 m_i R_0^2/B_0$ is the Alfvén time. In Tore Supra ohmic shots, $T_0 = 2.4 \times 10^3$ keV and $n_0 = 3.3 \times 10^{19} \mathrm{m}^{-3}$ yield a Lundquist number $S_{TS} = 2 \times 10^8$. Increasing S automatically increases computing time, so that it is difficult to use $S > 10^7$. In the following, the value $S = 10^7$, 20 times too small, is assumed. The amplitude of diamagnetic effects is tuned by the parameter $\alpha = m_i R_0/(ZeB_0 \tau_A)$. The experimental value in the Tore Supra shot #44634 is $\alpha_{TS} = 0.08$. However, at $S = 10^7$, the threshold in α needed to achieve the regime of accelerated reconnection is slightly higher, so we used $\alpha = 0.10$ in our simulations. Since S is smaller than the experimental value, the dynamics of sawtooth cycles is faster, and the transport coefficients must be rescaled accordingly. However, realistic values of the pinch velocity and particle diffusion coefficient in the core are numerically challenging, so the values $D_\perp a^2/\tau_A = 2 \times 10^{-7}$ and $|V_p|/V_A = 6 \times 10^{-8}$ have been used. This values of $D_\perp$ and $|V_p|$ depart significantly from the experimental ones, but the density profile is still peaked enough to allow qualitative comparisons with the experiment.

At this point, it is useful to note that there is no constraint in the code to restore the safety factor and pressure profiles to their initial values. Thus, the code computes the profiles self-consistently after each reconnection phase and the initial profiles are never recovered. As a result, the first reconnection phase, which features depend on the initial profiles, is irrelevant.

The density source is an edge-localized restoring source of the form $S_n = -\nabla \cdot (D_\perp \nabla n_0)$; n_0 being the initial density. Since the initial density profile is flat inside the $q = 1$ surface and decreases monotonically to 70% of its core value at the edge, the source is vanishing inside the $q = 1$ surface during the whole simulations. Only the inside of the $q = 1$ surface is studied, so that the particle source is neglected in the following. The input pinch velocity V_p profile is defined such as to reproduce the experimental profile measured in Ref. 34. For practical reasons, it could be measured only in the region $r < 0.1$ m, with an approximately constant value for $0.05\ \mathrm{m} < r < 0.1\ \mathrm{m}$. The constant value was extrapolated for $r > 0.1$ m.

B. 2D advection-diffusion code

In order to directly study the transport of the density in the poloidal plane by the combination of flow advection and diffusion, a simple bi-dimensional cylindrical code has been written. The convective flow is supposed to be the sum of a potential velocity of the form $\mathbf{v} = \hat{\mathbf{z}} \times \nabla \phi$, z being the symmetry direction of the system, and of a radial pinch velocity V_p, designed in the same way as in XTOR-2F. The diffusion coefficient $D_\perp$ is assumed constant. Thus, the following equation is solved:

$$\partial_t n + (\hat{\mathbf{z}} \times \nabla \phi) \cdot \nabla n + \nabla \cdot (n V_p) = D_\perp \nabla_\perp^2 n. \quad (6)$$

The code uses an implicit finite differences second order in space Arakawa scheme on a cartesian mesh with Dirichlet boundary conditions on a circle.

IV. NUMERICAL RESULTS

A. Introduction

As explained in Sec. II, experimental results suggest that the density and temperature behave differently. Namely, the temperature evolves smoothly after the crash while the density is found to exhibit very specific structures.[39] This fact can be surprising considering the typical assumption that the temperature and the density are both flux functions in ohmic plasmas: $T_e = T_e(\psi)$; $n = n(\psi)$ where ψ is a flux surface label, which will shortly be defined precisely. This assumption generally holds in a steady-state fusion plasma. However, it does not hold in the regions subject to important MHD activity, for instance close to the $q = 1$ surface during a sawtooth precursor or postcursor kink, not to mention during the crash itself.

Let us briefly review the arguments leading to the conclusion that n and T_e are flux functions. To clarify the notations, we use a reduced MHD model close to Strauss model.[40] We take the magnetic field to be $\mathbf{B} = B_T \hat{\mathbf{e}}_\varphi + \nabla\psi \times B_T$, with $B_T = I/R$ the toroidal field, and I is constant up to order 2 in the inverse aspect ratio ε. The magnetic potential is $A = \psi_T(r)\hat{\mathbf{e}}_\theta + \psi B_T$, the poloidal flux is $\psi_p = I\psi$, and the toroidal flux ψ_T is independent of time. The velocity is $\mathbf{v} = \hat{\mathbf{e}}_\varphi \times \nabla\Phi/B^2 + v_\parallel \mathbf{B}/B$, where Φ is the electric potential. The projection of the ideal Ohm's law on B_T yields the following equation:

$$\partial_t \psi = -\frac{R^2}{I} \nabla u \cdot (\nabla r \times \nabla \Phi \times \nabla \psi) + O(\varepsilon^2). \quad (7)$$

The equilibrium flux is denoted by ψ_0, and perturbed quantities are denoted by a tilde, and depend on ψ_0 and the variable $\chi = \theta - u - \omega t$. When the equilibrium is perturbed, $\psi = \psi_0 + \tilde{\psi}$, the flux surface label is the helical flux

$$\psi_\star = \frac{\delta_{\psi_0}}{\delta 1 - q(\psi)/n} \, d\psi + \tilde{\psi}.$$

Indeed the reader can check that $\mathbf{B} \cdot \nabla \psi_\star = 0$, using the relation $J^{-1} = \nabla u \cdot (\nabla\theta \times \nabla\psi_0) = 1/(qR^2)$. Note that the basis (ψ, θ, u) is indirect.

The helical function allows to write the Ohm's law in the form of a Poisson bracket

$$\partial_t \psi = \frac{R^2}{I} \nabla \cdot \left[\nabla \psi \times \nabla \left(\frac{\chi}{R^2} \right) \right]. \quad (8)$$

Equation (8) implies that the potential χ is such that

$$\chi = \chi_0(\psi) + F(\psi), \quad (9)$$

where F is an arbitrary function and $\chi_0(\psi_0)$ is solution to $\partial_t \psi + \{\chi_0, \psi\} = 0$. Using $\partial_t \psi = \partial_t \tilde{\psi}$ and $d\psi_0 = B_T r dr = d(q\psi)$, we find $\chi_0 = -\frac{1}{2} \omega B_T r^2$.

Finally, the magnetic operator $B \cdot \nabla$ can be written in terms of the helical flux

$$B \cdot \nabla f = \frac{I^2}{R^2} \{f, \psi\}. \quad (10)$$

Now, let us apply this formalism to the temperature and density evolution in the plasma. The argument for the temperature is straightforward. The parallel diffusion coefficient is large, so that Eq. (4), after expanding in terms of density and temperature, and using Eq. (2), the equation of evolution of the temperature at first order reduces to

$$\partial_t T_e = \chi_\parallel \nabla_\parallel^2 T_e \quad (11)$$

yielding $T_e(\psi)$. The other terms in the evolution of the temperature are perpendicular transport terms that control the details of the temperature profile across flux surfaces. To be more precise, Eq. (11) holds because the parallel diffusion time, $\tau_\parallel \sim 4\pi^2 R_0^2/\chi_\parallel$, is very short compared with the other time scales. Specifically, $\tau_\parallel$ must be large compared with the period of the mode, to guarantee adiabatic alignment of T_e on ψ. Typically, the ordering $\tau_\parallel^{-1} \ll \omega/2\pi$ holds. The other terms are either small curvature terms, either perpendicular diffusion terms, with characteristic time $\tau_\perp \sim a^2/\chi_\perp$, either terms related to drift advection with time $\tau_{ad} \sim a/V_E$. Since $V_E \sim 1\,\mathrm{km\,s^{-1}}$; $\chi_\parallel \sim 10^8\,\mathrm{m^2\,s^{-1}}$; $\chi_\perp \sim 1\,\mathrm{m^2\,s^{-1}}$, we have $\tau_\perp/\tau_\parallel \sim 10^5$ and $\tau_{ad}/\tau_\parallel \sim 10^2$.

The argument for the density is slightly more subtle, because homogenization on flux surfaces can arise from two processes: parallel homogenization by sound-waves or by $E \times B$ drift convection. To simplify the discussion, we neglect curvature terms in a low inverse aspect ratio limit. The source vanishes in the center. Then, Eq. (2) can be recast at lowest order in ϵ into

$$\partial_t n + \frac{\omega}{B_T} \cdot \nabla \chi \times \nabla n + v_\parallel \nabla_\parallel n + n \nabla_\parallel v_\parallel = \nabla \cdot D_\perp \nabla n. \quad (12)$$

The advection by $v_\parallel$ is usually negligible, the right hand side corresponds to slow dynamics, so we are left with two terms, the advection by the electric drift velocity and the parallel compressibility.

If the latter is dominant, then coupling with the momentum equation (3) yields the physics of sound waves with dispersion relation $\partial_t^2 n = c_s^2 \nabla_\parallel^2 n$, with $c_s = \sqrt{T_e/m_i}$ the ion speed of sound. In the case of non perturbed flux surfaces, the latter equation yields the dispersion relation $\omega^2 = k_\parallel^2 c_s^2$, where $k_\parallel = 1/R(1/q - 1)$. Thus, the density tends to become a flux function, if the wave is sufficiently fast compared to the frequency of the mode. Any perturbation with non-vanishing parallel wave-number is propagated along the field line and homogenization on the flux surface occurs.

If, however, the advection by the electric drift velocity dominates, then n will be constant on the streamlines of the flow. Here, it is important to note that the stream function is not χ, in the same sense that $\tilde{\psi}$ was not the flux label. To be an acceptable stream function, the potential $\chi^{(1)}$ involved in the electric drift needs to be independent of time. Thus, the stream function is obtained in the frame moving with the perturbation at the pulsation ω. This change of frame introduces a Doppler shift in the potential: $\chi^{(1)} = \chi + r^2 \omega B_T/2$. We have indeed with this definition, up to $O(\epsilon^3)$ terms

$$(B \times \nabla \chi^{(1)})/B_T^2 = (B \times \nabla \chi)/B_T^2 - r\omega e_h,$$

and $\chi^{(1)}$ is independent of time because the new poloidal variable is $\theta^{(1)} = \theta - \omega t$. If ideal MHD is valid, Eq. (9) implies that

$$\chi^{(1)} = \chi - \chi_0 = F(\psi). \quad (13)$$

Finally, when advection dominates, the density tends to being a function of $\chi^{(1)}$, which is a flux function, and the density ends up being a flux function. This expresses the frozen-in-law.

However, when there is significant MHD activity in the plasma, the previous arguments for the density break down for different reasons. First, non-ideal MHD effects become important in a narrow layer around the radius of the $q = 1$ surface, where the assumption $\chi = F(\psi)$ breaks down. More importantly, it takes some time for a scalar to homogenize on flux surfaces. If the time scales of evolution of the MHD instability (which can be very short in the non-linear phase of the sawtooth, for example) are faster than typical homogenization time, then the final state of the scalar can be significantly different from a flux function.

Let us now turn to the influence of these MHD effects on the transport of particles in the poloidal plane.

B. Flattening by the postcursor mode

In this subsection, a standard non-ideal single fluid MHD model is assumed, even if the mode is supposed to have a frequency of the order of the diamagnetic frequency. The nature and structure of the flow associated with a saturated kink mode is described. The bifluid effects are important only in the next subsection where the crescent-shaped structure is studied with the XTOR-2F code.

As noted in Sec. II, the strong flattening observed on the density profile occurs simultaneously with a saturated kink type $m/n = 1/1$ MHD mode. Let us first discuss the reasons that may lead to saturation rather than crash. For a kink mode, the linear drive depends on the details of the profiles inside the $q = 1$ surface, so that usually in the non-linear evolution the growth rate does not vanish and a crash occurs.

However, under certain condition, XTOR-2F exhibits a displaced helical $m/n=1/1$ equilibrium, where the kinked pressure is observed to rotate at almost constant frequency and a permanent reconnection layer forms.[38] This happens when diamagnetic effects are small, for instance in the beginning of the ramp phase, when the pressure gradient has not completely recovered its pre-crash value.

Here, we also use the MHD displacement ξ, which characterizes the mode. It is of the form $\xi(r,\theta,\varphi,t) = \xi_{1;1}(r)e^{-i(\omega t-m\theta+n\varphi)}$, together with the condition $\nabla\cdot\xi = 0$. The notations and assumptions are the same as in the introduction of this section. Thus, in the frame where ξ is defined, the equilibrium radial electric field vanishes, at least locally, and the flow associated with the mode has a velocity $v = d\xi/dt = \partial_t\xi = -i\omega\xi_{1;1}e^{-i(\omega t-m\theta+n\varphi)}$, where ω is the frequency of the mode. Let us note that the toroidal component of the displacement is $O(\varepsilon s)$ and contributes in $\nabla\cdot\xi$ only at order $O(\varepsilon s^2)$. Thus, it is neglected. Again, we use the electric potential $\Phi = \Phi_{1;1}(r)e^{-i(\omega t-m\theta+n\varphi)}$ associated with this flow, in a low inverse aspect ratio limit. Up to $O(\varepsilon)$ curvature terms, $v = (1/B^2)B\times\nabla\Phi = i(m/rB_T)\Phi e_r + (1/B_T)\partial\Phi/\partial\theta\, e_h$, so that $\Phi_{1;1}(r) = r\omega B_T\xi_r$. Consistency is ensured by the vanishing divergence conditions for both v and ξ. Thus, the flow is entirely determined by the shape of the MHD radial displacement. The possible shapes for the radial displacement ξ_r have been thoroughly studied and are well-known in many configurations. They stem from the minimization of a MHD energy functional with respect to the displacement ξ. Ideal MHD yields at lowest order a radial displacement that is a step function: constant for $r<r_s$ and vanishing for $r>r_s$. Addition of inertial effects in a narrow layer around the $q=1$ surface results in smoothing this step function. For instance, mere inertial effects yield a $\tan^{-1}$ function with characteristic width $d \sim r_s(\omega/\omega_A)^{1/3}/s$, where s is the magnetic shear at r_s; $s = (rq'/q)_{r_s}$.[9] Other authors studied the form of the displacement for a variety of current and pressure profiles, with addition of different non-ideal effects. More details can be found in Refs. 36, 41, and 42.

With the previously described shapes for ξ_r, Φ has the structure of two vortices in the poloidal plane, as seen on Fig. 5(a)), which represents the $m/n=1/1$ electric potential structure obtained with XTOR-2F in linear single fluid regime. However, Fig. 5(a)) is misleading because, as noted in the introduction of this section, $\partial_t\Phi = 0$. The stream function is obtained by moving to the frame where the perturbation is stationary, and adding the corresponding Doppler shift $r^2\omega B_T/2$. The streamlines are represented on Fig. 5(b)). They have indeed the same structure as the perturbed magnetic surfaces, confirming the results of the introductory subsection.

The amplitude of the flow is of the order of $\omega\xi_r$. Recall that here ω is the frequency of the mode and not its measured frequency X which is the sum of ω and of the Doppler shift due to the equilibrium $E\times B$ drift velocity. However, only the frequency in the laboratory frame X is measured. There are some measurements of the equilibrium radial electric field in Tore Supra using Doppler-shift measurements but they do not provide information below $r < 0.6$ m. Since we are interested in the electric field at the $q=1$ surface, here

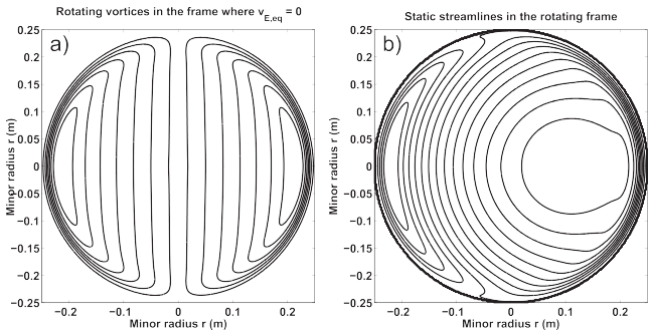

FIG. 5. Potential structure in the frame where $v_{E;eq}=0$ (a) and corresponding static streamlines of the flow in the rotating frame (b). The streamlines describe rotation around the displaced core, accelerated in the region of the $q=1$ surface.

$r \sim 0.3$ m, this is of no practical use. We could also estimate ω using the formula provided in Ref. 36, giving an expression, or at least a numerical resolution, for ω as a function of ω_i^2 and ω_e^2. However, these quantities are also difficult to evaluate on the $q=1$ surface because this corresponds to the radius where the profile turns flat, coming from the outside of the resonant surface. Thus, the computation of the gradient of the pressure profile involved in the evaluation of the diamagnetic frequencies is very imprecise.

Nonetheless, there is a way to get round this difficulty. First note that in the shot we are interested in, the density at the $q=1$ surface is much flatter than the temperature, thus $\omega_{\delta i;e}^2 \ll \omega_{T;\delta i;e}^2 = (\nabla B\times\nabla T_{\delta i;e})/(eB^2)$. Theoretical neoclassical results can be used to predict the value of the electric field as a function of the temperature gradient. Neoclassical theory in axisymmetric configurations does not allow to dissociate the electric field from the toroidal velocity in the force balance equation. In other words, only the quantity $E_r - v_u B_h$ can be computed, because the ambipolarity of the radial particle fluxes is automatically verified in this formalism. Neoclassical theory with magnetic ripple effects (the ripple is high in Tore Supra) removes this degeneracy and leads to the computation of the factor k_E of proportionality between the radial electric field and the ion temperature gradient: $E_r = k_E\partial_r T_i$. In other words, the Doppler shift $k\cdot v_E = -k_E\omega_i^2$. This factor of proportionality is determined by the competition between turbulence effects and ripple effects. The ripple plays an important role because it breaks axisymmetry and because it is responsible for local particle trapping leading to radial non-ambipolar particle fluxes. The electric field adjusts to compensate for this non-ambipolarity. In Tore Supra, it was found that ripple dominates, so that $k_E = 1.5$ (ripple plateau regime).[43,44] This result was checked experimentally in Ref. 45. Second, Ref. 36 allows straightforward evaluation of the kink pulsation in the case where $(\omega_{*i}/\omega_R)/(\omega_{*i}/\omega_H)^{1/3} \ll 1$, with $\omega_H = \omega_A/s$. In this case, $\omega = \omega_i^2/2$. For the situation under consideration, $\omega_A/S^{1/3} \ll 1$, and since we expect the shear to be small, the condition is marginally satisfied. Finally, we can write $|\omega| = |\omega_i^2/2 - k_E\omega_i^2|$, so $k_E = 1.5$ yields $\omega = -\omega_i^2$ and $\omega = \omega_i^2/2$. Thus, the kink pulsation is expressed without explicitly referring to the diamagnetic pulsation. This shows that the Doppler shift and the frequency of the mode play

comparable roles in the measured pulsation X of the mode. The Doppler shift and the mode frequency have opposite signs, and the existence of the mode reduces the pulsation to 2/3 of its value without kink activity. This shows that the 1 kHz frequency of the postcursor cannot be attributed to plasma rotation only, but that the mode's own frequency is of the order of 0.5 kHz, while the plasma rotates in the opposite direction at a frequency of the order of 1.5 kHz.

There is also some difficulty in estimating experimentally the amplitude of the radial displacement. It is straightforward only when the profiles are peaked since n_r is directly measurable as the displacement of the core. A typical core displacement for the saturated kink oscillation in Tore Supra ohmic shots is 0.1 m. At the onset of the crash, the core is displaced up to the $q = 1$ surface. The position of this surface r_s depends mainly on I_P. In the Tore Supra shot #44634, which characteristics are studied here, $I_P = 1.2$ MA, resulting in the $q = 1$ surface located at $r_s \simeq 0.3$ m. For the postcursor mode, there is usually no peaking in the core allowing to trace back the amplitude of the displacement. However, in our case, the peaking is seen to reappear while the kink oscillations are still present, so that its amplitude can be evaluated. It is of the order of 0.1 m, making the typical velocity of the order of 300 m s^{-1}.

However, the effective convection velocity can be much larger. The velocity along the line $\theta = 0$ is given by the expression

$$|v| = |v_\theta| = |\chi \partial n_r - r + r\partial_r n_r|;$$

so that the velocity is dominated by the term $\partial_r n$ near the $q = 1$ surface where the radial variations of n_r (and χ) are fast. This originates from the condition $\mathbf{r} \cdot \mathbf{n} = 0$. This can be seen on Figs. 5(a) and 5(b) where on the edges the streamlines are very close to each other, meaning significant acceleration of the flow. Fig. 6 represents the functions n_r versus $|n_r - r + r\partial_r n_r|$. It appears that the velocity is enhanced by a factor of 10 next to the $q = 1$ surface, compared with the rough estimate $v \sim \chi n_r$.

Now, let us use the advection-diffusion code described in Sec. III B to study the effects of this flow during 10 ms on the poloidal density profile. The stream function χ is obtained from XTOR-2F as the dominant $m/n = 1/1$ component of the potential in linear regime and without bifluid effects. The pinch velocity is set to zero in the 2D code because it does not play a role in the process, and χ is rescaled to be consistent with the measured MHD displacement. We take $r_s = 0.25$ m; $D = 0.05$ m^2 s^{-1}; $f = 400$ Hz; $n_r(r, \theta = 0) = 0.1$ m, the time step is 1 μs and the computation is done on a 256×256 cartesian grid. In order to reproduce the experimental results, we simply take an initial perturbation defined analytically by a smooth function of the form

$$n(r, \theta) = 1 + P(r)\frac{1 + \cos(\theta - \theta_0)}{2};$$

with $P(r) = 6r^4 - 2r^3 + r^2$. The precise expression of the initial perturbation is unimportant. The experimental perturbation could have been interpolated on the numerical mesh,

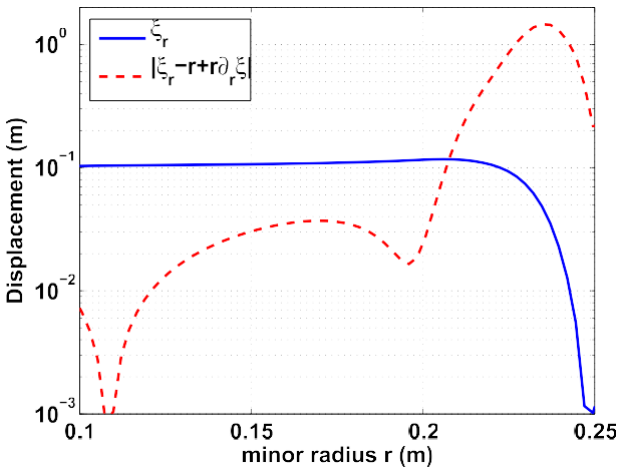

FIG. 6. Comparison between the radial displacement n_r and $|v_\chi| = |n_r - r + r\partial_r n|$ on the line $\theta = 0$.

but it would not have changed the discussion. Only a perturbation which is not a function of the potential is needed. The same simulation was done with other profiles and the results were similar.

The results of the advection simulation are presented in Fig. 7. It is seen that a frequency of 400 Hz and a MHD displacement of 0.1 m is sufficient to homogenize the density in the poloidal plane in 10 ms. The reason is that the velocity pattern enforces the density to enter the very thin zone where $\partial_r \chi$ is large, stretching the density profile. The characteristic width of the density "wall" generated by this process is small enough to be erased even by a small diffusion coefficient. By comparison, the purely diffusive evolution would have required a time of the order of 1 s to reach the same level of flatness.

C. The emergence of the crescent-shaped structure

In this subsection, the nature and the origin of the crescent-shaped structure observed after a sawtooth crash and described in Sec. II are investigated, using XTOR-2F sawtooth crash simulations. The results of the simulation are presented on Fig. 8. The time interval displayed spans a time of $8 \times 10^3 \tau_A$, longer than the reconnection time itself, approximately $3 \times 10^3 \tau_A$. The crash presented here is the third one in a series of four (not mentioning the first irrelevant one), which display quite regular behaviour. The sawtooth period τ_{ST} is $\tau_{ST} \simeq 4 \times 10^4 \tau_A$, which translates to almost 10 ms, close to the experimental value in Tore Supra ohmic discharges, 20–40 ms, with $\tau_A \simeq 2 \times 10^{-7}$ s. However, one should not forget that τ_{ST} increases with the Lundquist number S, almost linearly for smaller S. Recall that S in XTOR-2F is 20 times smaller than the experimental value, so that our sawtooth period may actually be overestimated compared to the experimental one. The similarity of Fig. 8 with Fig. 2 is striking. The same crescent-shaped structure is obtained at the end of the reconnection phase. As in the experiment, it is encircled by a secondary ring-shaped structure. Namely, frame I^0 of Fig. 8 looks much like frame E of Fig. 2. It is possible to trace back the apparition of the density structures using the outputs of the code.

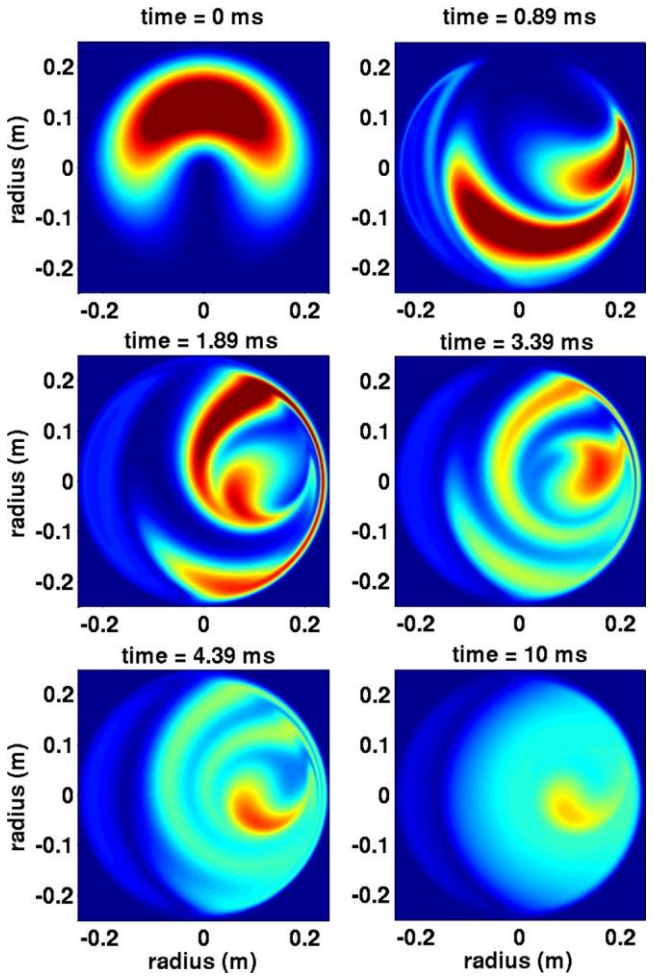

FIG. 7. Advection diffusion simulation with $r_s = 0.25$ m; $D = 0.05$ m^2 s^{-1}; $f = 400$ Hz; $n_r(r = 0) = 0.1$ m. Homogenization occurs in less than 10 ms.

- A^0: The density poloidal profile before kink destabilization.
- B^0: Initial core displacement pushing the core toward the $q = 1$ surface. A thin density structure is already distinguishable in the right part of the image.
- C^0 and D^0: Formation of circular structures is clearly visible while the dense core shrinks at the reconnection layer.
- E^0: Reconnection rate is enhanced due to diamagnetic effects and leads to a gap (dark blue) and bump (dark red on the right edge of the image) structure.
- F^0 and G^0: The process continues and finally reconnection stops. The result is that the core density has been remapped on a circular zone close to the separatrix.
- H^0: The density structure homogenizes poloidally to form a ring and feeds a more internal crescent-shaped structure.
- I^0: While the external ring structure slowly diffuses, the remaining dominant density structure is crescent-shaped.

The origin of this density redistribution can be understood using the same kind of arguments as in the previous subsection. Indeed, the poloidal perpendicular flows are, again, the key to understand this phenomenon. The sequence displayed on Fig. 8 corresponds to one magnetic reconnection event. As noted before, the kink displacement is accompanied by rapid flows emerging from the reconnection layer, located at r_s. When reconnection occurs, these flows are Alfvénic. However, the corresponding Alfvén speed is composed using the reduced helical field, $B_h^2 = B_\theta(1 - q)$; $|j_B| = rB_T(1 - q)/(Rq)$. The maximum value of $|j_B|/B_T$ inside the $q = 1$ surface is of the order of 3×10^{-3}, given that $(1 - q_0) > 0.1$ and $r_s/R_0 > 0.1$. Actually, the velocity of the jet generated at the separatrix reaches the value of $0.01 V_A$ when reconnection is at its maximum rate. It is a very fast velocity, considering that the Alfvén velocity is of the order of 10^7 m s^{-1}. To understand how the density is transported by the flows, it is necessary to evaluate the different terms in Eq. (2) during the simulation, while the structure develops. However, this must be done in the rotating frame, because in the laboratory frame a significant part of the time derivative of the density is due to the term $r\dot{x}e_h\, n_r$ which overrides important information. Since the simulations presented here have bifluid effects included, we must take into account the total velocity $v_i = v_E + v_{\parallel i} + v_i^*$. Here, $v_E = v_E - r\dot{x}e_h$, but we will further remove the tilde notation for clarity. Recall that in a cylindrical plasma, the diamagnetic flux does not advect the density at all, $nv_i^* \cdot \nabla n = 0$. In a toroidal plasma, however, the compressibility of the diamagnetic velocity does not totally compensate the advection, $\nabla \cdot (nv_i^*) = 1/e\,\nabla p_i \cdot \nabla \times (B/B^2) \neq 0$. This term actually turns out to be dominant in the continuity equation, especially in the singular layer, where the pressure gradient is significantly enhanced. It is mainly compensated by the divergence of the electric drift velocity, that is, we have

$$1/e\,\nabla p_i \cdot \nabla \times (B/B^2) = -n\,\partial/\partial r \cdot \nabla \times (B/B^2); \qquad (14)$$

except in the resonant layer. Equation (14) is an expression of the fact that ion confinement is electrostatic.

The sum of these two terms is curvature terms. The next dominant term in the continuity equation is the electric drift advection $v_E \cdot \nabla n$. In the following, the contributions of the curvature terms and of the electric drift advection during the reconnection phase are compared. The different dominant terms in the continuity equation are plotted in Fig. 9 across one minor radius, for one given angle, here $\theta = p/4$ at $t = 126914\, s_A$, corresponding to frame E^0 in the region of the growing perturbation ($\theta = 0$ is on the equatorial plane). In Fig. 9(b), the sum of the two terms from Fig. 9(a) is plotted in blue. The electric advection term is also represented in green, while the red curve represents the sum of the blue and green curves, representing the dominant term in the time derivative of the density in the rotating frame.

It can be concluded from Fig. 9(b) that in the reconnection region, the density evolution is driven by the electric velocity, which is not surprising given the amplitude of the flow. Indeed the main contribution to the red curve is the green curve, and it adds positively in the l.h.s. of Eq. (2), that is, it is a density sink, at the origin of the deep gap observed on frame E^0. The same curves can be plotted for any angle θ. Fig. 10 is at the angle $\theta = 0$, which corresponds to the right end of the reconnection layer. Here, it is seen that the dominant term is made from curvature, or compressibility effects, and adds negatively to the density balance equation. It is a

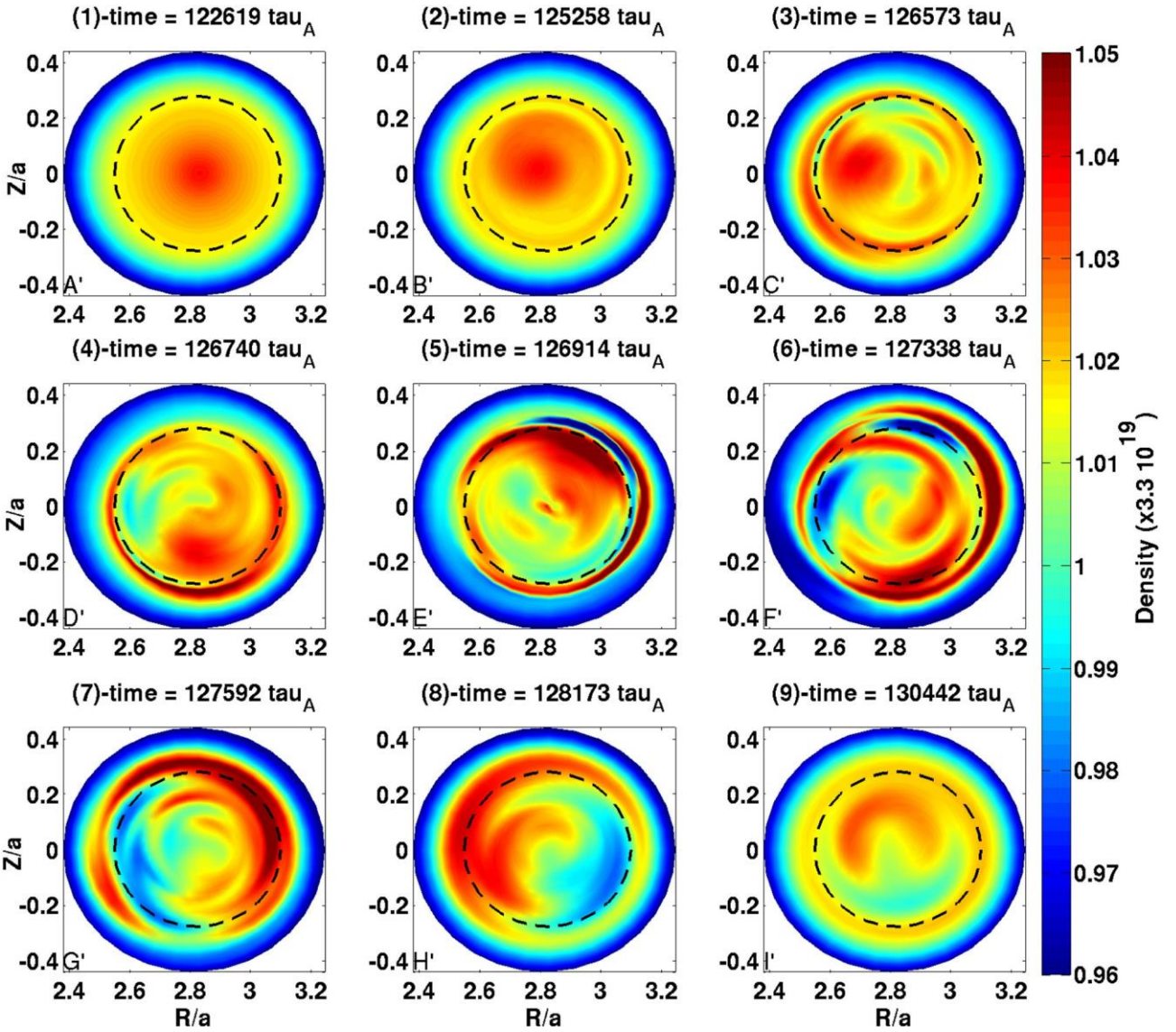

FIG. 8. Colour plots of the density in an XTOR-2F sawtooth crash simulation. The crescent-shaped structure is recovered and forms during the crash. Rotation is counter-clockwise. The dotted black circle figures the position of the initial $q=1$ surface. It should not be confused with the separatrix which moves outward during reconnection.

source of density and leads to the formation of the bump observed on frame E′.

Fig. 11 helps summarize the process described using Figs. 9 and 10. The stream function of the flow is displayed together with the separatrix at $t=126914\ s_A$, when the reconnection flows are the largest, and it is compared with a Poincaré plot of the magnetic surfaces. The stream function adopts the same general structure as the magnetic flux

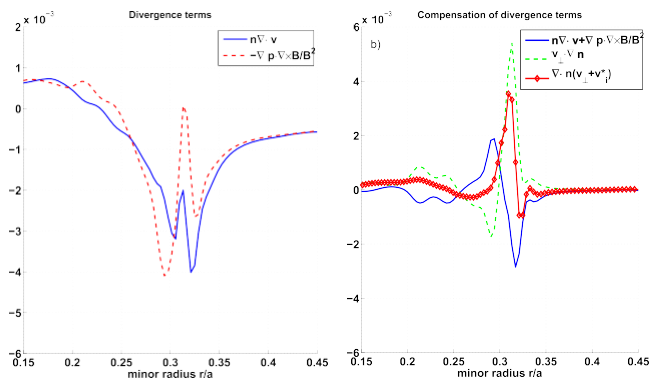

FIG. 9. Plot of the different terms in the continuity equation, for $h=p=4$; $t=126914\ s_A$.

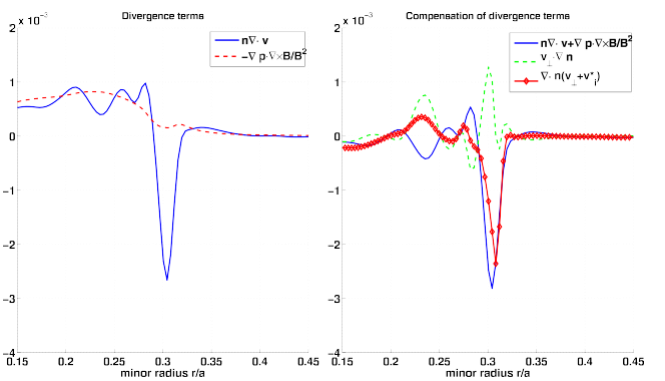

FIG. 10. Plot of the different terms in the continuity equation, for $h=0$; $t=126914 s_A$.

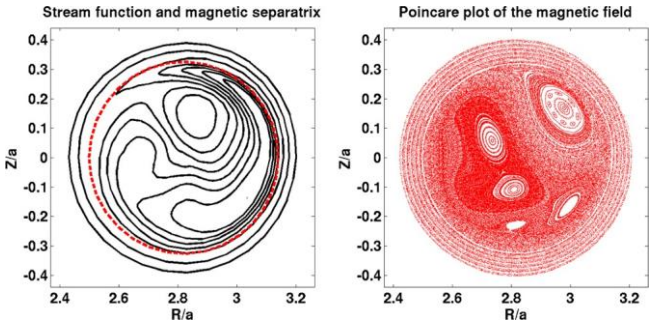

FIG. 11. Contours of the potential function in the rotating frame during the crash, with the magnetic separatrix shown in red at time $t = 126914\ s_A$ (a). It is compared with the magnetic surfaces obtained as Poincaré plots (b). The stream function and the flux label display similar structures.

surfaces, a bubble-shaped old core and a wide island encircling it, with a few secondary islands denoting $m/n = 2/1$ and $m/n = 3/3$ activity. It is clearly seen on Fig. 11(a) how advection lets the density cross the separatrix to map the dense core on a circular zone outside the $q = 1$ surface.

The analysis of Figs. 9–11 leads to the following conclusions:

- The particles are mainly advected by the fast electric drift velocity jets generated at the reconnection layer.
- After crossing the separatrix, finite compressibility leads to a density build-up producing the observed ring-shaped structure.

It is more difficult to understand how the more central crescent-shaped structure is generated. A first guess would be that it corresponds merely to an $m = 1$ perturbation of the density profile, thus uninteresting when looking at the radial transport properties linked with the sawtooth crash. However, the structure remains visible on the poloidally averaged profiles (as seen on Fig. 12), so this possibility is ruled out. Instead, the structure really seems to be fed by the outer ring (frame I^0). Following the end of the reconnection phase, the magnetic island occupying the volume inside the separatrix must become a new magnetic core. Thus, magnetic surfaces must recenter, carrying with them the plasma in a radial motion.

Fig. 11 reveals that during reconnection, the structure and position of the magnetic island approximately correspond to the structure seen on the stream function. Following the arguments of Sec. IV B, one could expect to see flattening occur on the magnetic island, resulting in a final flat density profile, in accordance with the most common sawtooth model (see, for example, Ref. 14). However, there is a major difference between the situation studied presently and Sec. IV B: while the flattening process was due to the existence of a long-lasting potential structure, giving the density enough time to whirl several times around the vortex, now the whole process lasts only one reconnection time. The most significant part of the reconnection phase happens in less than $2 \times 10^3\ s_A$, with a typical period of rotation around the vortex of $10^3\ s_A$ (only immediately in the reconnection layer and for a short time does the velocity reach the value $0.01 V_A$), so homogenization does not have time to occur.

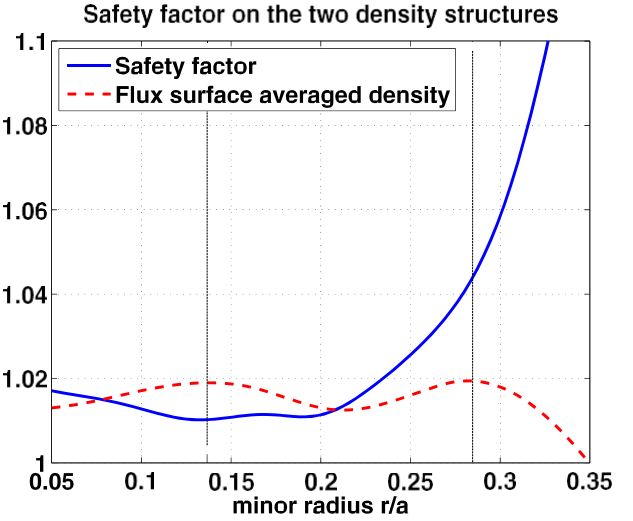

FIG. 12. Safety factor and density on the line $\eta = p$ at $t = 130442\ s_A$. The dotted vertical lines show the radial location of the two structures. Safety factor and normalized density have same units on the y-axis.

V. DISCUSSION

It is meaningful to compare XTOR-2F results and the experimental results displayed in Sec. II. Frames E and F of Fig. 2 show that the crescent-shaped structure homogenizes in a few milliseconds. The external structure also homogenizes, and two rings remain. This is consistent with sound-wave homogenization, occurring on a time scale $s_s = (k_\parallel c_s)^{-1}$. Given the post-crash temperature of 2.2 keV, a homogenization time of a few milliseconds is consistent with a $dq = \eta j = -1$ in the range $[10^{-2}; 10^{-1}]$. In the experiment, the safety factor is not known with a sufficient precision to conclude definitively, even if such values correspond to commonly observed magnetic shearing rates. In XTOR-2F, reconnection is complete, so that the safety factor is above 1 in all the plasma after the crash. Fig. 12 shows the safety factor and the flux surface averaged density at the time $t = 130442\ s_A$, frame I^0 of Fig. 8. It is seen that $q - 1$, and hence $k_\parallel$, is approximately 5 times bigger on the external structure than on the crescent. Hence, it homogenizes poloidally 5 times faster, in a few s_s; $\sim s_s$ $0.5 \times 10^3 s_A$. Thus, the transition from crescent to ring is not observed for the more central structure because since the Lundquist number is lower than in the experiment, the sawtooth cycle dynamics is faster and the next crash occurs before homogenization is complete.

A difference with the experiment is the amplitude of the final structures. In the experiment, the crescent's amplitude is of the order of 2% of the total density, while the amplitude of the circular structure is less than 1%. In XTOR-2F, these amplitudes are both slightly below 1% (after flux surface average). In both cases, the circular structure in the final state is located very close to the $q = 1$ surface.

It is crucial to note that our sawtooth crash model implies that a significant part of the density in excess of the density at the $q = 1$ surface is not expelled, contrary to what is usually assumed.[14] The crescent-shaped structure is the trace of a reinjection mechanism. It does not matter much for

the electron density because the structure represents a very small part of the total density. However, one is tempted to apply this model to impurities like tungsten or helium, which have different profiles. A typical helium profile almost vanishes at the $q=1$ surface, if one assumes efficient pump out, while the helium produced by fusion reactions in the deepest core builds up inside the $q=1$ surface. If a significant part of the particles is not expelled but reinjected by the flows inside the $q=1$ surface, it could lead to insufficient helium (and/or tungsten) exhaust. The following simplistic model clarifies this point. In theory, one can measure the reinjection ratio of a species s, f_s, defined by the ratio

$$f_s = \frac{N_{p;s}(r_{inv};\, t_1)}{N_{p;s}(r_{inv};\, t_0)};$$

where

$$N_{p;s}(r;\, t) = \int_0^{\rho(r)} n_s(r;\, t) - n_s(r_{inv};\, t_0)\, J\, dr\, d\theta\, d\varphi;$$

($J = 1/[\nabla r \cdot (\nabla\theta \times \nabla\varphi)]$) is the number of particles inside the surface of radius r, in excess of $n_s(r_{inv};\, t_0)$; t_0 and t_1 are two instants immediately before and after the crash. Here, $n_s(r_{inv};\, t_0)$ designates the density of the species s at the inversion radius of the sawtooth at t_0. Actually, reinjection may be an inappropriate term since it is not completely clear whether the density is reinjected at the end of the reconnection phase or if simply some part of it does not cross the separatrix. Nonetheless, we will stick to this terminology. In general, $0 < f_s < 1$, since 0 corresponds to full flattening, and 1 corresponds to no net particle flux through the inversion radius between the beginning and the end of the crash. If one assumes similar density redistribution mechanisms for electrons and minority ions, then the ratios f_e and f_{He} are the same. A number N_{He}^0 of α particles are produced during two sawtooth crashes. If we denote by $N_{He}(n)$ the number of α particles inside the $q = 1$ surface immediately after the nth sawtooth crash, then $N_{He}(n+1) = f_{He}(N_{He}(n) + N_{He}^0)$. It follows that

$$\frac{N_{He}(n)}{N_{He}^0} \underset{n\to\infty}{\to} \frac{f_{He}}{1 - f_{He}} > f_{He}.$$

Hence, for non-negligible ratio f_{He}, the density inside the $q = 1$ surface can be significantly enhanced by the $1/(1 - f_{He})$ factor.

The most important caveat to this model is that the reinjection ratio f_s is not a well-defined quantity. Indeed, it is very sensitive to the choice of t_0 and t_1, and to the measurement of the position of the inversion radius. In particular, it is difficult to define a density inversion radius in our simulations. Indeed, the concept is most easily defined if the profile following the crash is flat in the region of the $q = 1$ surface, however, in our case, the circular structure ends up in the region of the $q = 1$ surface, as seen on frame I[0] of Fig. 8, and has the same amplitude as the crescent. Thus, it is meaningless to compute f_e in this case. However, in the experiment, the crescent largely dominates over the ring, which is consistent with the experimental results of Ref. 34 showing that the fluctuation level $\delta n/n$ is reduced inside the $q = 1$ surface. Remembering that the ring originates from the density circular pulse following the separatrix, it is more affected by diffusion, which explains its diminished size. Also, the inversion radius is easier to define and the time scales of sawtooth global dynamics and sawtooth crash are well separated, allowing a reasonable choice of t_0 and t_1 for each crash. The measured ratio f_e depends on the crash. The sequence in Fig. 2 is part of a sequence of 5 tomographically analyzed crashes. The ratios f_e measured for this subsequence are plotted in Fig. 13. It is seen that typically, $0.2 < f_e < 0.5$. Given that the redistribution mechanism is dominated by the flows coupled to diffusion, the ratios of the different species are likely to be similar, except if the turbulent diffusion coefficients are very different. Even if a more precise study is beyond the scope of this article, our results imply that impurity transport in sawtooth regime is a serious issue which deserves closer investigations.

The previous sections allow to reconstruct a full story of the evolution of the density, and how it is coupled to the sawtooth evolution. The experimental results, confirmed by nonlinear MHD simulations, lead to the following conclusions:

- At the onset of the sawtooth crash, the hot and dense core is driven toward the $q=1$ surface, where it is advected by fast electric drift velocity jets on the separatrix. The temperature is also advected by the electric drift, however, its evolution is dominated by a large diffusivity, so that it remains constant on the magnetic surfaces.
- After the crash, about one third of the particles have been reinjected inside the initial $q=1$ surface in the form of a crescent-shaped structure. Depending on the amplitude of the remaining MHD activity, two evolutions are possible:
  (1) When there is low activity after the crash, there is a smooth evolution dominated by sound waves, which homogenize the density in the poloidal direction and lead to a double ring-shaped density structure, on top of which the pinch term builds a peaking of the profile.
  (2) When a long-lived MHD mode with frequency comparable to the kink frequency persists after the crash,

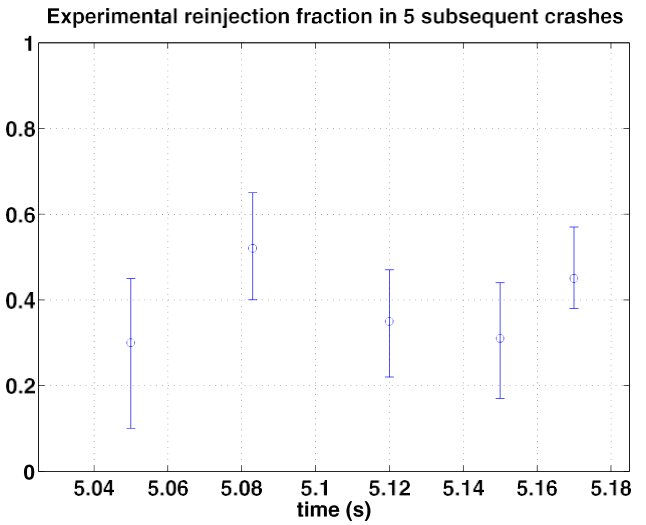

FIG. 13. Reinjection ratios in the experiment for 5 subsequent sawtooth crashes. They are plotted at the time of the corresponding crash.

the potential pattern drives a rapid flattening of the profiles because of the existence of a strong velocity shear zone next to the $q=1$ surface. This flattening occurs because initially the density is not a flux function. Thus, the flows, which are tangent to the potential and magnetic surfaces, redistribute the density to make it a flux function, and at the end of this convection process the density ends up to be flat. However, the temperature, which is already a flux function, is not significantly affected by these flows.

As a final remark, note that the structure described in this paper should not be mixed up with the crescent-shaped structure observed in Ref. 19 using soft X-ray tomography. In this paper, the structure is described as a relic of the old core, diffused on time scales longer than the electron temperature time scale, located across the separatrix and attributed to metallic impurities. Here instead, the crescent is observed directly on the electron density clearly inside the $q=1$ radius, and results from the dynamic redistribution of the density profile during the sawtooth collapse, due to the strong reconnection flows.

VI. CONCLUSION

The results of this paper can be summarized as follows.

Recent experimental results obtained with a novel fast-sweeping X-mode reflectometry technique give access to fine density structures in ohmic plasmas. These structures are tightly linked to the sawtooth dynamics. The electron density and temperature are found to evolve differently: whereas the time scales of the sawtooth (0.1–1 ms) are long compared to the temperature parallel diffusivity time scale (~ 10 ls), they are of the same order of magnitude as the time scales ruling the density inside the $q=1$ surface.

The differences in temperature and density behavior are not due to a decoupling between the electric potential and the magnetic flux function. In the simulation, the potential tends to be a flux function, in accordance with the theoretical structure of the kink flow.

A significant density flattening has been shown to be consistent with the kink expected during postcursor oscillations. The ratio between the frequency of the postcursor and the frequency measured in the laboratory frame was determined using neoclassical theory.

The density is found to be redistributed inside the poloidal plane, with a reinjection ratio of the order of 0.3. The XTOR-2F non-linear and bifluid full MHD code recovers the observed structures.

ACKNOWLEDGMENTS

The authors would like to thank F. Halpern and R. Guirlet for fruitful discussions. This work, supported by the European Communities under the contract of Association between EURATOM and CEA, was carried out within the framework of the European Fusion Development Agreement. The views and opinions expressed herein do not necessarily reflect those of the European Commission.

[1]A. Aydemir, Phys. Fluids B 4, 3469 (1992).
[2]D. Biskamp and J. F. Drake, Phys. Rev. Lett. 73, 971 (1994).
[3]D. Biskamp and T. Sato, Phys. Plasmas 4, 1326 (1997).
[4]M. N. Bussac, R. Pellat, D. Edery, and J. L. Soule, Phys. Rev. Lett. 35, 1638 (1975).
[5]I. T. Chapman, R. Scannell, W. A. Cooper, J. P. Graves, R. J. Hastie, G. Naylor, and A. Zocco, Phys. Rev. Lett. 105, 255002 (2010).
[6]R. Kleva, Phys. Fluids B 3, 102 (1991).
[7]R. Kleva, J. Drake, and F. Waelbroeck, Phys. Plasmas 2, 23 (1995).
[8]B. Rogers and L. Zakharov, Phys. Plasmas 3, 2411 (1996).
[9]M. Rosenbluth, R. Dagazian, and P. Rutherford, Phys. Fluids 16, 1894 (1973).
[10]F. Waelbroeck, Phys. Fluids B 1, 2372 (1989).
[11]X. Wang and A. Bhattacharjee, Phys. Rev. Lett. 70, 1627 (1993).
[12]L. Zakharov, B. Rogers, and S. Migliuolo, Phys. Fluids B 5, 2498 (1993).
[13]R. Hastie, Astrophys. Space Sci. 256, 177 (1997).
[14]F. Porcelli, D. Boucher, and M. N. Rosenbluth, Plasma Phys. Controlled Fusion 38, 2163 (1996).
[15]O. Sauter, E. Westerhof, M. L. Mayoral, B. Alper, P. A. Belo, R. J. Buttery, A. Gondhalekar, T. Hellsten, T. C. Hender, D. F. Howell, T. Johnson, P. Lamalle, M. J. Mantsinen, F. Milani, M. F. F. Nave, F. Nguyen, A. L. Pecquet, S. D. Pinches, S. Podda, and J. Rapp, Phys. Rev. Lett. 88, 105001 (2002).
[16]S. Hu and G. Iley, in *Proceedings of the International Atomic Energy Agency (IAEA) Technical Committee Meeting on Alpha Particles in Fusion, Aspenas (Sweden)*, 1991.
[17]C. Shin, G. H. Miley, and C. E. Singer, Fusion Technol. 33, 387 (1998).
[18]F. Imbeaux and Y. Peysson, Phys. Rev. Lett. 84, 2873 (2000).
[19]Y. Nagayama, K. M. McGuire, M. Bitter, A. Cavallo, E. D. Fredrickson, K. W. Hill, H. Hsuan, A. Janos, W. Park, G. Taylor, and M. Yamada, Phys. Rev. Lett. 67, 3527 (1991).
[20]D. Wróblewski and R. T. Snider, Phys. Rev. Lett. 71, 859 (1993).
[21]C. Janicki, R. Décoste, and C. Simm, Phys. Rev. Lett. 62, 3038 (1989).
[22]H. K. Park, N. C. Luhmann, A. J. H. Donné, I. G. J. Classen, C. W. Domier, E. Mazzucato, T. Munsat, M. J. van de Pol, Z. Xia, and TEXTOR Team, Phys. Rev. Lett. 96, 195003 (2006).
[23]H. K. Park, A. J. H. Donné, N. C. Luhmann, I. G. J. Classen, C. W. Domier, E. Mazzucato, T. Munsat, M. J. van de Pol, Z. Xia, and TEXTOR Team, Phys. Rev. Lett. 96, 195004 (2006).
[24]G. Taylor, E. Fredrickson, B. Grek, R. Goldston, D. Johnson, H. Park, J. Schivell, F. Stauffer, R. Wieland, and M. Zarnstorff, Nucl. Fusion 29, 3 (1989).
[25]H. Bindslev, S. K. Nielsen, L. Porte, J. A. Hoekzema, S. B. Korsholm, F. Meo, P. K. Michelsen, S. Michelsen, J. W. Oosterbeek, E. L. Tsakadze, E. Westerhof, P. Woskov, and TEXTOR Team, Phys. Rev. Lett. 97, 205005 (2006).
[26]R. Sabot, A. Sirinelli, J.-M. Chareau, and J.-C Giaccalone, Nucl. Fusion 46(9), S685 (2006).
[27]R. Sabot, in *37th EPS Conference on Plasma Physics*, Dublin, Ireland (2010).
[28]H. Lütjens and J.-F. Luciani, J. Comput. Phys. 229, 8130 (2010).
[29]H. Lütjens and J.-F. Luciani, J. Comput. Phys. 227, 6944 (2008).
[30]H. Lütjens, J.-F. Luciani, D. Leblond, F. Halpern, and P. Maget, Plasma Phys. Controlled Fusion 51, 124038 (2009).
[31]By "rotation" frequency, it is meant the part of X which is due to the Doppler shift $k \cdot v_{E;eq} : X = \omega - k_h E_r/B$.
[32]Y. Nagayama, R. Buchse, A. Cavallo, E. Fredrickson, A. Janos, K. Mcguire, G. Petravic, C. Sule, and G. Taylor, Rev. Sci. Instrum. 61, 3265 (1990).
[33]A. A. Ware, Phys. Rev. Lett. 25, 15 (1970).
[34]R. Guirlet, A. Sirinelli, T. Parisot, R. Sabot, J. F. Artaud, C. Bourdelle, X. Garbet, P. Hennequin, G. T. Hoang, F. Imbeaux, J. L. Segui, D. Mazon, and D. Villegas, Nucl. Fusion 50, 095009 (2010).
[35]W. Houlberg, K. Shaing, S. Hirshman, and M. Zarnstorff, Phys. Plasmas 4, 3230 (1997).
[36]G. Ara, B. Basu, B. Coppi, G. Laval, M. Rosenbluth, and B. Waddell, Ann. Phys. (N.Y.) 112, 443 (1978).
[37]F. D. Halpern, H. Lütjens, and J.-F. Luciani, Phys. Plasmas 18, 102501 (2011).
[38]F. D. Halpern, D. Leblond, H. Lütjens, and J.-F. Luciani, Plasma Phys. Controlled Fusion 53, 015011 (2011).
[39]It must be noted, however, that the density diagnostic is more precise than the temperature diagnostic.
[40]H. Strauss, J. Plasma Phys. 57, 83 (1997).

[41]M. Bussac and R. Pellat, Phys. Rev. Lett. 59, 2650 (1987).
[42]H. Deblank and T. Schep, Phys. Fluids B 3, 1136 (1991).
[43]X. Garbet, J. Abiteboul, E. Trier, O. Gurcan, Y. Sarazin, A. Smolyakov, S. Allfrey, C. Bourdelle, C. Fenzi, V. Grandgirard, P. Ghendrih, and P. Hennequin, Phys. Plasmas 17, 072505 (2010).
[44]X. Garbet, G. Dif-Pradalier, C. Nguyen, Y. Sarazin, V. Grandgirard, and P. Ghendrih, Phys. Plasmas 16, 062503 (2009).
[45]C. Fenzi, X. Garbet, E. Trier, P. Hennequin, C. Bourdelle, T. Aniel, G. Colledani, P. Devynck, C. Gil, O. Guercan, L. Manenc, M. Schneider, J. L. Segui, and T. S. Team, Nucl. Fusion 51, 103038 (2011).